19th Brazilian Congress of Thermal Sciences and Engineering
November 6th–10th, 2022, Bento Gonçalves - RS - Brazil

ENC-2022-0031
Kinetic theory based lattice-Boltzmann models for multiphase systems

Maria Rosa Amorim Faria Lisboa
Pontifical Cathtolic University of Paraná. R. Imaculada Conceição, 1155 - Prado Velho. Paraná/Curitiba.
lisboa.maria@pucpr.edu.br
Diogo Nardelli Siebert
Federal University of Santa Catarina. R. Dona Francisca, 8300 - Zona Industrial Norte. Joinville/Santa Catarina.
diogo.siebert@ufsc.br
Paulo César Philippi
Pontifical Cathtolic University of Paraná. R. Imaculada Conceição, 1155 - Prado Velho. Paraná/Curitiba.
paulo.philippi@pucpr.br

Abstract. *The Lattice Boltzmann Method (LBM) is a viable alternative to study multiphase systems due to its mesoscopic scale, based on kinetic theory. This makes LBM capable of recovering the fluid flow macroscopic behavior, while also describing the interface formation induced by intermolecular interaction in multiphase systems. For this reason, a variety of multiphase LBM models are found in the literature. However, the interface region is still an issue for computer simulations due to its high-density gradients. Most models suffer from one or more numerical problems, such as instability, truncation errors, discretization errors, and/or high-order moment effects. As a result, most simulations present either parasitic currents, artificial interfacial tension, or anisotropy. To avoid these obstacles, some authors employ heuristic strategies that do not fit into the kinetic theory framework of LBM. The present work is a comparative study of two multiphase LBM models with a solid physical foundation in accordance with the kinetic theory. The first model is due to He* et al. *(1999) and based on two distribution functions that retrieve the order parameter and the pressure as their zeroth-order moments, using a D2Q9 velocity set. The second model is due to Siebert* et al. *(2014) and based on a single distribution function for density, employing a D2V17 velocity set. The simulations provide density profiles, pressure profiles, vapor-liquid coexistence curves and interface tension charts, for each model. As well as they evaluates the suitability for phase change and simulations of the Rayleigh-Taylor instability.*

Keywords: *LBM, Multiphase flow, Interface, Liquid-vapor model*

1. INTRODUCTION

Multiphase systems are comprised of one or more components that present themselves in different phases. In this work, only single component systems consisting of liquid and vapor will be addressed. Hence, the entire system behaves according to a single phase diagram and, for every temperature below the critical temperature, there are two coexistent equilibrium densities. Intermolecular forces are responsible for phase segregation and interface formation. For a given temperature, the intensity of these intermolecular interactions is responsible for the interface thickness.

Due to the relevance of this topic, a wide variety of lattice-Boltzmann models (LBM) for liquid-vapor multiphase systems have been proposed in the last decades. However, these models are limited to low density ratios due to numerical instabilities at the interface (Inamuro *et al.*, 2004). In addition, some models have other undesired effects, such as the presence of spurious currents, thermodynamic inconsistencies (Shan and Chen, 1994), lack of Galilean invariance (Swift *et al.*, 1996), and artificial interface tension (Kikkinides *et al.*, 2008). To avoid these undesired effects, the literature presents a variety of solutions, including practical but heuristic propositions, as well as options that have a sound physical foundation but distance themselves from the kinetic theory framework of LBM. This paper aimed to identify and analyze models based on the kinetic theory, such as the models proposed by He *et al.* (1999) and Siebert *et al.* (2014).

He *et al.* (1999) developed a model for multiphase flow in the incompressible limit. The authors incorporate intermolecular interactions and use two distribution functions through a change of variables. According to the authors, the change of variable grants greater numerical stability. This formulation reached density ratios up to the order of 20, with well-defined density profiles (Lee and Lin, 2005). Moreover, the authors were able to simulate Rayleigh-Taylor instabilities, obtaining results that agree with theoretical predictions.

A typical Rayleigh-Taylor instability (RTI) occurs when a heavier fluid sits on top of a lighter fluid under the effect of

gravity, characterizing an unstable interface. As the heavy fluid goes down, the RTI develops spikes with a characteristic mushroom shape along with the appearance of "plumes" flowing upwards. At the same time, the light fluid forms bubbles as it goes up to occupy the place of the heavy fluid. It receives its name after Lord Rayleigh, who was the first to study this phenomenon in the 19th century, and later Sir G. I. Taylor in the 1950s (Tryggvason, 1988).

In 2014, Siebert *et al.* also proposed a model based on kinetic theory applying concepts very similar to the ones found in He *et al.* (1999). Furthermore, the authors used a nondimensionalization strategy that allows the adjustment of the interface thickness and interface tension in an independent way. The model achieved density ratios up to 90, and it has been validated by retrieving the coexistence curve and interface density profiles as well as measuring the interface tension compared to theoretical values. Nevertheless, it has never been used to simulate an RTI before.

Since 1999, many authors have studied the model proposed by He *et al.* (1999). According to these studies, this method has an artificial interface tension (Kikkinides *et al.*, 2008) and there are debates about the physical meaning of the pressure throughout the deduction of the model (Huang *et al.*, 2015). Some authors like Zhang *et al.* (2000) and Chao *et al.* (2011) suggested some changes and improvements to the model. However, this work seeks to analyze the change of variables used by He *et al.* (1999) in their original article, as well as investigate how this method allows the simulation of a Rayleigh-Taylor instability. Thus, it was aimed to reproduce the vapor-liquid models proposed by He *et al.* (1999) and Siebert *et al.* (2014), comparing them and analyzing the strategies employed by the authors.

2. BACKGROUND AND METHODOLOGY

The kinetic theory describes the dynamics of gas on a mesoscopic scale, which can be interpreted as a statistical description of a large number of particles (Kruger *et al.*, 2017). Consider the kinetic equation:

$$\partial_t f + \boldsymbol{\xi} \cdot \boldsymbol{\nabla}_{\mathbf{x}} f + \frac{\mathbf{F}^g}{\rho} \cdot \boldsymbol{\nabla}_{\boldsymbol{\xi}} f = \Omega(f), \tag{1}$$

where f is a distribution function for the population of molecules, t is the time, $\boldsymbol{\xi}$ is the molecular velocity vector, $\mathbf{F^g}$ is a body force, ρ is the density, and Ω is a collision operator. This equation describes the advection of f with molecular velocity $\boldsymbol{\xi}$, under the effect of a body force and collisions with other molecules.

For ideal monoatomic gases, the atoms collide elastically resulting in a sharp change in their velocity (Kruger *et al.*, 2017). When dealing with ideal fluids, there is no long-range interaction between molecules and each particle is considered as a material point. For this reason, molecular interaction and the volume of molecules needs to be added when considering non-ideal fluids. The intermolecular interaction is a consequence of their electrostatic nature, and it may be approximated from the average attraction potential between them (He *et al.*, 1998). Then, we add the Enskog volume exclusion term as a correction when the particles are modeled as hard spheres, resulting in an intermolecular force field $\mathbf{F}$ (He *et al.*, 1998):

$$\mathbf{F} = \rho\boldsymbol{\nabla}(2a\rho + \kappa\nabla^2\rho) - \boldsymbol{\nabla}(\rho RT(b\rho\chi)), \tag{2}$$

where a is the intermolecular force parameter corresponding to the equation of state, b is the co-volume, related to the volume occupied by a particle, κ is an interface parameter, R is the ideal gas constant, and T is the temperature. The parameter χ indicates the increase in collision probability due to the increase in fluid density (He *et al.*, 1999). For the van der Waals equation of state, $\chi = \frac{1}{1-b\rho}$ (Philippi *et al.*, 2012).

He *et al.* (1998) proposed to incorporate the interaction force into the body force therm Eq. 1. After these force is added to the equation and a multiple-scale analysis of Eq. 1 is made, the linear momentum balance macroscopic equation is retrieved in the form:

$$\partial_t(\rho\mathbf{u}) + \boldsymbol{\nabla} \cdot (\rho\mathbf{u}\mathbf{u} + P_s\boldsymbol{\delta} + \boldsymbol{\tau}) = \mathbf{G} - \boldsymbol{\nabla} \cdot \mathbf{S}, \tag{3}$$

where $\mathbf{u}$ is the macroscopic velocity, $\boldsymbol{\tau}$ us the viscous stress tensor, $\mathbf{G}$ is the gravity force. The Korteweg tensor $\mathbf{S} = \kappa\boldsymbol{\nabla}\rho\boldsymbol{\nabla}\rho$ and $P_s = P - \kappa\rho\nabla^2\rho - \frac{\kappa}{2}(\boldsymbol{\nabla}\rho)^2$ is a scalar pressure, in which P is the thermodynamic pressure. Therefore, Eq. 3 describes the flow's macroscopic linear momentum advection and diffusion, considering two sources: gravity and interaction between molecules.

2.1 Model 1: He *et al.* (1999)

He *et al.* (1999) proposed an athermal model for multiphase systems in the incompressible limit. In this sense, the authors base themselves on Eq. 3 and added an incompressibility hypothesis. The model employs two distribution functions, including one to track the pressure. This pressure distribution function g is introduced through a change of variables that reads: $g = fRT + \psi\Gamma(0)$ in which ψ is the excess pressure of a non-ideal gas when compared to an ideal gas pressure:

$$\psi(\rho) = P - \rho RT = \rho RT(b\rho\chi) - a\rho^2, \tag{4}$$

P is the thermodynamic pressure given by any non-ideal equation of state, and $\Gamma(\mathbf{u})$ corresponds to the Maxwell-Boltzmann equilibrium distribution, described in:

$$\Gamma(\mathbf{u}) = \left(\frac{1}{2\pi RT}\right) exp\left[-\frac{(\boldsymbol{\xi}-\mathbf{u})^2}{2RT}\right]. \tag{5}$$

Thereby, the force term given by Eq. (2). may be rewritten as a function of ψ and the surface force $\mathbf{F}_s = \kappa\rho\boldsymbol{\nabla}\nabla^2\rho$ as:

$$\mathbf{F} = -\boldsymbol{\nabla}\psi(\rho) + \mathbf{F}_s. \tag{6}$$

Considering an incompressibility hypothesis, $\boldsymbol{\nabla}\cdot\boldsymbol{u} = 0$, it may be observed that:

$$\partial_t\psi(\rho) + \boldsymbol{\xi}\cdot\boldsymbol{\nabla}\psi(\rho) = (\boldsymbol{\xi}-\mathbf{u})\cdot\boldsymbol{\nabla}\psi(\rho). \tag{7}$$

Then, the Boltzmann equation for the distribution g is derived according to:

$$\partial_t g + \boldsymbol{\xi}\cdot\boldsymbol{\nabla}_{\boldsymbol{x}} g = \Omega(g) + (\boldsymbol{\xi}-\mathbf{u})\cdot[\Gamma(\mathbf{u})(\mathbf{F}_s+\mathbf{G}) + (\Gamma(\mathbf{0})-\Gamma(\mathbf{u}))\boldsymbol{\nabla}\psi(\rho)], \tag{8}$$

while the equilibrium distribution g^{eq} is given by: $g^{eq} = \rho RT\Gamma(\mathbf{u}) + \psi(\rho)\Gamma(\mathbf{0})$.

The second distribution function h tracks the index function ϕ, which establishes a linear relation with ρ that reads:

$$\rho(\phi) = \rho_l + \frac{\phi-\phi_l}{\phi_h-\phi_l}(\rho_h-\rho_l), \tag{9}$$

where ϕ is the index function and the labels h and l indicate that the property corresponds to the heavy and light fluid, respectively. This way, the Boltzmann equation for h is defined as:

$$\partial_t h + \boldsymbol{\xi}\cdot\boldsymbol{\nabla} f = \Omega + \frac{(\boldsymbol{\xi}-\mathbf{u})}{RT}\cdot(-\boldsymbol{\nabla}\psi)\Gamma(\mathbf{u}), \tag{10}$$

and the equilibrium distribution h^{eq} is given by: $h^{eq} = \phi\Gamma(\mathbf{u})$.

The discretization for these equations were made in accordance with He *et al.* (1999), with a second order approximation for the streaming term, a D2Q9 velocity set, and a simple BGK collision operator, such as $\Omega(f) = -\frac{f_i - f_i^{eq}}{\tau}$, in which τ is the relaxation time. The D2Q9 velocity set comprises a bidimensional space with 9 velocities as in Fig. 1.

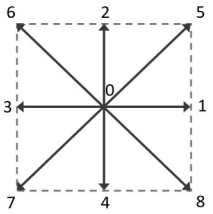

$$e_i = \begin{bmatrix} 0 & 0 \\ 1 & 0 \\ 0 & 1 \\ -1 & 0 \\ 0 & -1 \\ 1 & 1 \\ -1 & 1 \\ -1 & -1 \\ 1 & -1 \end{bmatrix} \qquad W_i = \begin{bmatrix} \frac{16}{36}, i = 0 \\ \frac{4}{36}, i = 1,2,3\ e\ 4 \\ \frac{1}{36}, i = 5,6,7\ e\ 8 \end{bmatrix}$$

Figure 1. D2Q9 velocity set's vector and matrix representation, and weights W_i.

An explicit dimensionless discrete form is obtained for the algorithm, by defining $\overline{g}_i(\mathbf{x},t) = g_i^*(\mathbf{x},t) - \frac{1}{2}[\Omega(\mathbf{x},t) + S_i^{g*}(\mathbf{x},t)]$, where S_i^{g*} is the last term on Eq. (8), and $\overline{h}_i(\mathbf{x},t) = h_i^*(\mathbf{x},t) - \frac{1}{2}[\Omega(\mathbf{x},t) + S_i^{h*}(\mathbf{x},t)]$, where S_i^{h*} is the last term on Eq. (10). This way, Eq. (8) and Eq. (10) are rewritten according to:

$$\begin{aligned}\overline{g}_i(\mathbf{x}+\mathbf{e}_i\delta_t, t+\delta_t) = \quad & \overline{g}_i(\mathbf{x},t) - \frac{\overline{g}_i(\mathbf{x},t) - g_i^{*eq}(\mathbf{x},t)}{\tilde{\tau}} \\ & + \left(1-\tfrac{1}{2\tilde{\tau}}\right)(\mathbf{e}_i - \mathbf{u}^*(\mathbf{x},t))\cdot[\Gamma_i^*(\mathbf{u}^*)(\mathbf{F}^*{}_s + \mathbf{G}^*) - (\Gamma_i^*(\mathbf{u}^*) - \Gamma_i^*(\mathbf{0}))\boldsymbol{\nabla}^*\psi^*],\end{aligned} \tag{11}$$

$$\overline{h}_i(\mathbf{x}+\mathbf{e}_i\delta_t, t+\delta_t) = \overline{h}_i(\mathbf{x},t) - \frac{\overline{h}_i(\mathbf{x},t) - h_i^{*eq}(\mathbf{x},t)}{\tilde{\tau}} + \left(1-\frac{1}{2\tilde{\tau}}\right)(\mathbf{e}_i - \mathbf{u}^*(\mathbf{x},t))\cdot\frac{\boldsymbol{\nabla}^*\psi^*}{c_s^2}\Gamma^*(\mathbf{u}^*). \tag{12}$$

where * indicates the dimensionless variables, $c_s = 1/\sqrt{3}$ for the D2Q9 velocity set and $\tilde{\tau} = \tau^* + 0.5$. In this work, the dimensionless variables were defined as a function of the critical density ρ_c,the system temperature T and the mesh parameters: the distance between nodes h and the time step δ_t. Note that the pressure P^* and parameter κ^* is given by $P^* = P\frac{\delta_t^2}{\rho_c h^2}$ and $\kappa^* = \kappa\frac{\rho_c\delta_t^2}{h^4}$.

The kinematic viscosity ν in the model is given by $\nu = (\tilde{\tau}-0.5)c_s^2$ and the moments of interest can be recovered by:

$$\sum_i \overline{h}_i = \phi, \tag{13}$$

$$\sum_i \overline{g}_i = P^* + \frac{1}{2}\mathbf{u}^*\cdot\boldsymbol{\nabla}^*\psi^*, \tag{14}$$

$$\sum_i \overline{g}_i \mathbf{e}_i = \rho^* c_s^2 \mathbf{u}^* - \frac{1}{2} c_s^2 (\mathbf{F}_s^* + \mathbf{G}^*). \tag{15}$$

Equilibrium distributions can be rewritten with the help of Hermite polynomials, resulting in:

$$\Gamma^*(\mathbf{u}^*) = W_i \left[1 + \frac{1}{c_s^2} u_\alpha^* e_{i,\alpha} + \frac{1}{2c_s^2} (u_\alpha^* u_\beta^*) \left(\frac{1}{c_s^2} e_{i,\alpha} e_{i,\beta} - \delta_{\alpha\beta} \right) \right], \tag{16}$$

$$h_i^{*eq} = \phi^* \Gamma^*(\mathbf{u}^*), \tag{17}$$

$$g_i^{*eq} = \rho^* c_s^2 \Gamma^*(\mathbf{u}^*) + W_i \psi^*. \tag{18}$$

The equations above were written in Einstein notation, in which α and β, refer to the x and y directions and $\delta_{\alpha\beta}$ is the Kronecker delta operator. Note that, $P^* = \psi^* + \rho^* c_s^2$ so Eq. (18) can also be written according:

$$g_i^{*eq} = W_i P^* + \rho^* c_s^2 [\Gamma^*(\mathbf{u}^*) - 1]. \tag{19}$$

2.2 Model 2: Siebert *et al.* (2014)

Siebert *et al.* (2014) developed a model for non-ideal fluids in multiphase single-component systems. This model employs strategies similar to the model by He *et al.* (1999) to introduce intermolecular interactions and recover equivalent macroscopic equations. However, it uses a single distribution function to track the density, directly. In this sense, the Boltzmann equation can be written as Eq. (20) and equilibrium distribution f^{eq} is defined according to:

$$\partial_t f + \boldsymbol{\xi} \cdot \boldsymbol{\nabla}_{\boldsymbol{x}} f = \Omega(f) + \frac{(\boldsymbol{\xi} - \mathbf{u})}{RT} \cdot [\mathbf{G}^* + \boldsymbol{\nabla}(\rho RT - P) + \mathbf{F}_s] \, \Gamma(\mathbf{u}), \tag{20}$$

$$f^{eq} = \rho \Gamma(\mathbf{u}). \tag{21}$$

In accordance with the 2014 paper by Siebert *et al.*, this work will use a D2V17 velocity set and a second order discretization for the advective term. The D2V17 velocity set comprises a bidimensional space with 17 velocities as in Fig. 2, considering $c_s = \sqrt{\frac{72}{125+5\sqrt{193}}}$.

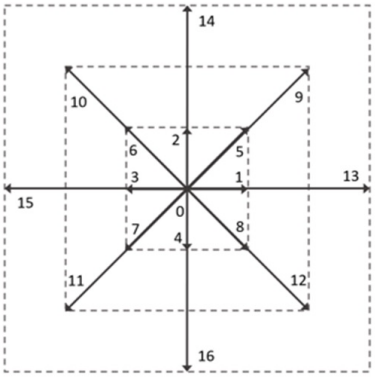

$$e_i = \begin{vmatrix} 0 & 0 \\ 1 & 0 \\ 0 & 1 \\ -1 & 0 \\ 0 & -1 \\ 1 & 1 \\ -1 & 1 \\ -1 & -1 \\ 1 & -1 \\ 2 & 2 \\ -2 & 2 \\ -2 & -2 \\ 2 & -2 \\ 3 & 0 \\ 0 & 3 \\ -3 & 0 \\ 0 & -3 \end{vmatrix} \qquad W_i = \begin{bmatrix} 0.402005, & i = 0 \\ 0.116155, & i = 1,2,3,4 \\ 0.0330064, & i = 5,6,7,8 \\ 0.0000790786, & i = 9,10,11,12 \\ 0.000258415, & i = 13,14,15,16 \end{bmatrix}$$

Figure 2. D2V17 velocity set's vector and matrix representation, and weights W_i.

In its explicit dimensionless discrete form, Eq. (20) and Eq. (21) are rewritten as:

$$\begin{aligned} \overline{f}_i(\mathbf{x} + \mathbf{e}_i \delta_t, t + \delta_t) &= \overline{f}_i(\mathbf{x}, t) - \frac{\overline{f}_i(\mathbf{x},t) - f_i^{*eq}(\mathbf{x},t)}{\tilde{\tau}} \\ &+ \left(1 - \tfrac{1}{2\tilde{\tau}}\right) \frac{(\mathbf{e}_i - \mathbf{u}^*(\mathbf{x},t))}{\rho^* c_s^2} \cdot \left[\mathbf{G}^* + c_s^2 \boldsymbol{\nabla}_{\boldsymbol{x}^*} (\rho^* - \varsigma P^*) + \rho^* \boldsymbol{\nabla}_{\boldsymbol{x}^*} (\kappa^* \nabla_{x^*}^2 \rho^*) \right] f_i^{*eq}(\mathbf{x}, t), \end{aligned} \tag{22}$$

$$\begin{aligned} f^{*eq} = \rho^* W_i \Big[1 + \tfrac{1}{c_s^2} u_\alpha^* e_{i,\alpha} &+ \tfrac{1}{2c_s^2} (u_\alpha^* u_\beta^*) \left(\tfrac{1}{c_s^2} e_{i,\alpha} e_{i,\beta} - \delta_{\alpha\beta} \right) \\ &+ \tfrac{1}{6c_s^6} (u_\alpha^* u_\beta^* u_\gamma^*) \left(e_{i,\alpha} e_{i,\beta} e_{i,\gamma} - c_s^2 (\delta_{\alpha\beta} e_{i,\gamma} + \delta_{\alpha\gamma} e_{i,\beta} + \delta_{\beta\gamma} e_{i,\alpha}) \right) \Big]. \end{aligned} \tag{23}$$

The nondimensionalization of model 2 is slightly different than the one for model 1. The dimensionless variables were defined as a function of the critical density ρ_c, the critical pressure P_c, the system temperature T, and the mesh parameters.

The terms $\varsigma = \frac{P_c}{\rho_c RT}$ and $\upsilon = \rho_c\sqrt{\frac{\kappa}{P_c}}$ arise in the process and are related to the critical properties and interface behavior of the model. The authors demonstrate that the interface thickness, as well as the interface tension, can be regulated using ς and υ as parameters. In this case, the pressure $P^* = \frac{P}{P_c}$ while κ^* keeps the previous definition but adds the relation $\kappa^* = \varsigma\upsilon^2 c_s^2$.

The kinematic viscosity ν in the model is given by $\nu = (\tilde{\tau} - 0.5)c_s^2$. Density and velocity can be recovered through zeroth- and first-order moments as in:

$$\sum_i \overline{f}_i = \rho^*, \tag{24}$$

$$\sum_i \overline{f}_i \mathbf{e}_i = \rho^* \mathbf{u}^* - \frac{1}{2}\left(\mathbf{G}^* + c_s^2 \boldsymbol{\nabla}_{x^*}(\rho^* - \varsigma P^*) + \mathbf{F}_s^*\right). \tag{25}$$

3. RESULTS AND DISCUSSIONS

The vapor-liquid coexistence curves were compared for each model, as well as the density profile, obtained for the flat interface and a static drop. Then, it was checked if the models agrees with the Young-Laplace law. The resulting interface tension were compared with theoretical values. The models were also evaluated for their ability to handle phase transitions and simulate Rayleigh-Taylor instabilities.

The insertion of molecular interaction within the model aim to describe interface formation and motion. One way to evaluate the interface in the model is to compare the interfaces properties obtained by numerical simulation with the theoretical prediction. With this in mind, the interface density profile, thickness λ, and tensionγ can be mathematically described, respectively, by:

$$y = \sqrt{\frac{\kappa}{2}}\int_{\overline{\rho}}^{\rho} \frac{d\rho}{\sqrt{H(\rho)}}, \tag{26}$$

$$\lambda = (\rho_h - \rho_l)\sqrt{\frac{\kappa}{2H(\overline{\rho})}}, \tag{27}$$

$$\gamma = \int_{-\infty}^{\infty} \sqrt{\kappa 2H(\rho)}d\rho. \tag{28}$$

where y is a coordinate for the interface profile, $\overline{\rho}$ is the average density and H is the excess of Helmhotlz free energy defined by $H = \frac{\kappa}{2}\left(\frac{d\rho}{dy}\right)^2$ (Philippi, 2022).

As mentioned, g_i^{*eq} can be calculated by either Eq. (18) or Eq. (19). Thus, when using Eq. (18), the model will be called 1A and when using Eq. (19), the model will be referred as 1B.

It is also noteworthy that, He *et al.* (1999) disregarded the surface force in all the simulations presented by the authors. Therefore, in this work, $\kappa = 0$ was also adopted in the simulations performed with model 1, except when mentioned otherwise. In all simulations presented for model 2, κ was set to 0.1. This way, the interface resolution λ is defined as a function of the critical pressure P_c.

3.1 Coexistence curve

To evaluate the coexistence curves, simulations were performed with a flat interface and periodic boundary conditions, for each model. When the equilibrium was reached, the densities of each phase were measured. The stopping condition adopted was the squared difference of the pressure, between two subsequent time intervals, being less than or equal to 9×10^{-7}.

For this simulation, the results for models 1A and 1B were similar, when $\kappa = 0$. One may notice that Model 2 does not converge to the analytical value as the width of interface increases. The discrepancies observed in the vapor branch can be reduced by employing a third-order discretization of the advective term. Figure 3 presents a comparison between the models. Note that model 2 reached lower values for T_r and therefore higher density ratios.

3.2 Density profile in a plane interface

Next, density profiles were taken on a flat interface. Figure 4(a) presents the density profile obtained for the reduced temperature T_r of 0.95 for models 1A with different interface resolutions in comparison with the theoretical profile given by Eq. (26). Figure 4(b) shows the same for model 2 with $T_r = 0.95$ and 0.80.

Model 1B's interface density profile does not agree with the theoretical prediction, with a much smoother interface. For model 1A and model 2, the interface resolution showed a good fit, with little interference in the profile. Once again, it is noteworthy that model 2 can achieve a better fit if a third order discretization for the advective term is used, as showed by Siebert *et al.* (2014).

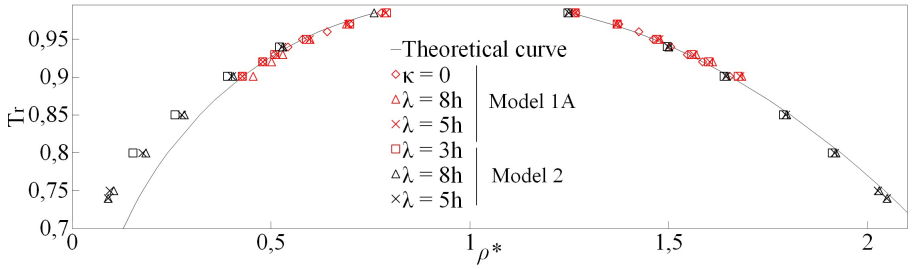

Figure 3. Coexistence curve for models 1 and 2, with a variety of interface resolutions, in comparison to the theoretical curve given by the van der Waals equation of state.

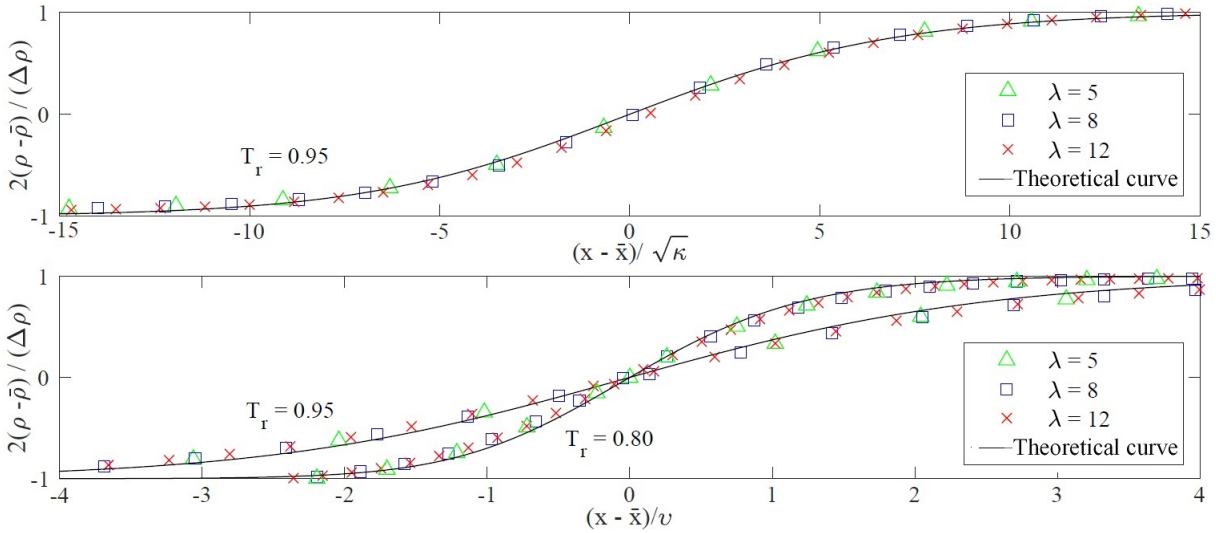

Figure 4. Comparison of density profiles with the theoratical curve given by Eq. 26, with a variety of interface resolutions for (a) model 1A and (b) model 2.

3.3 Static droplet

To test the isotropy of the models, a simulation was carried out with a square droplet. It was expected that, by the end of the simulation, the droplet should become circular. For model 1A and for model 2, all the droplets simulated reached a circular shape until the end of the simulation, as shown in Fig. 5(b). On the other hand, for model 1B, it was not possible to simulate a static droplet in a satisfactory way.

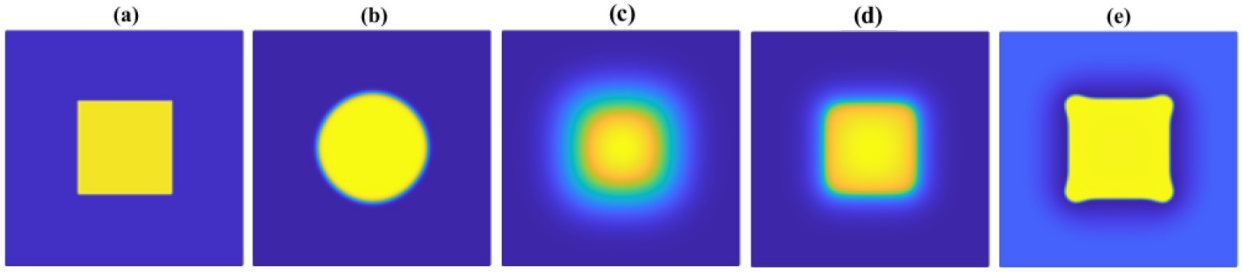

Figure 5. Square droplet at (a) the beginning of simulation, (b) the end of simultaion at $T_r = 0.97$, according to Model 1A; (c) the end of simultaion at $T_r = 0.97$ according to Model 1B; (d) the end of simultaion at $T_r = 0.95$ according to Model 1B; and (e) the end of simultaion at $T_r = 0.90$ according to Model 1B;

For $T_r > 0.95$, model 1B does not reach equilibrium. At this temperature, the droplet's interface progressively increases in thickness, as shown Fig. 5(c). For $T_r = 0.95$, the droplet kept the interface well defined, however, it displays anisotropic behavior, as shown in Fig. 5(d). While for $T_r < 0.95$, Fig. 5(e) shows that the anisotropy worsens, deforming the droplet.

A comparison of the resulting density profiles at different density ratios for each model is illustrated in Fig. 6. In general, the results show a thicker interface when closer to the thermodynamic critical point. As for model 1B, the reduced temperature T_r seems to have a significant impact on the shape of the interface.

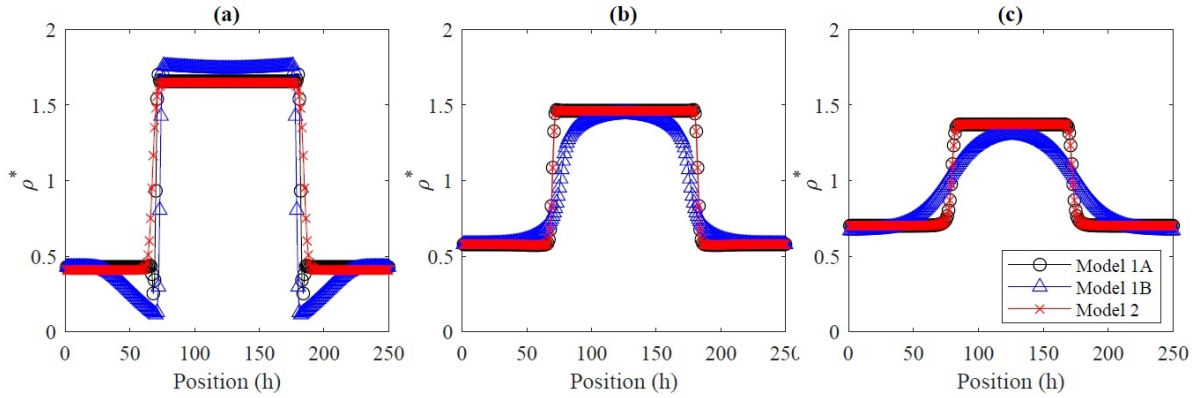

Figure 6. Density profile comparison for each model at different T_r. (a)$T_r = 0.90$, (b)$T_r = 0.95$ and (c)$T_r = 0.97$.

The pressures obtained were equivalent or within close range of the theoretically predicted thermodynamic pressures P_{th}, as shown in Fig. 7. Model 1A and model 2 presented pressure variation in the interface region, due to the density gradient and according to the equation of state. As expected, this effect is greater the lower the reduced temperature, although, model 1A displayed some irregularities for lower T_r values, around 0.90. For model 1B, the pressure profiles obtained are constant, consistent with the saturation pressure predicted by Maxwell's area rule.

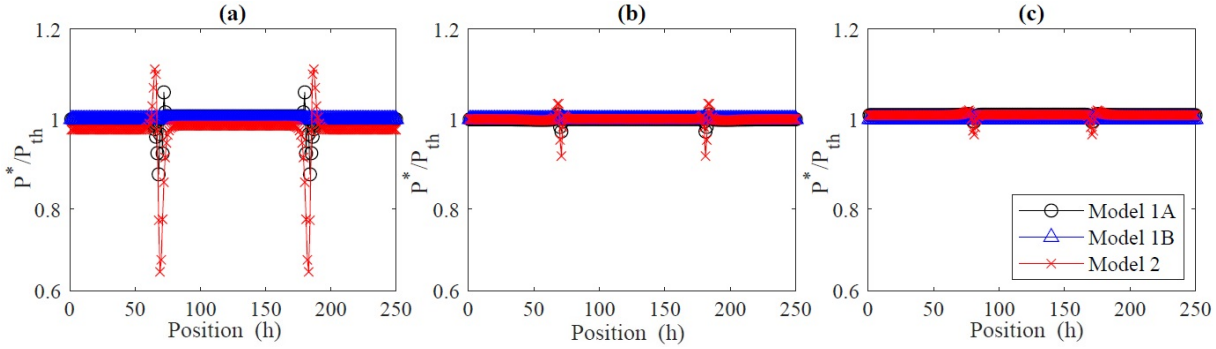

Figure 7. Pressure profile comparison for each model at different T_r. (a)$T_r = 0.90$, (b)$T_r = 0.95$ and (c)$T_r = 0.97$.

3.4 Young-Laplace Test

According to the two-dimensional Laplace's law, a droplet in equilibrium must follow the relation given by: $\Delta P = \frac{\gamma}{R}$, in which ΔP is the pressure difference between the liquid and vapor phase, γ is the interface tension and R is the radius of the droplet (Kruger *et al.*, 2017). Thus, the pressure variation in the droplet must have a linear relationship with the inverse of its radius. To verify this relation, the Young-Laplace test was performed on each model.

It was possible to measure the artificial interface tension for $\kappa = 0$ in model 1A, as shown in Tab. 1. The artificial interfacial tensions obtained represent about 10% of the theoretical interface tension for their respective temperature. Figure 8(a) illustrates the Young-Laplace test result for $\kappa \neq 0$, for interface thicknesses λ of 3h and 5h. Figure 8(b) shows a comparison of the measured interface tension and the the theoretical curve according to Eq. 28.

Table 1. Interfacial tension for model 1A, $\kappa = 0$.

T_r	$\gamma^*_{theoret.}$	$\gamma^*, for \kappa = 0$	$\gamma^*/\gamma^*_{theoret.}$
0.90	0.2834	0.0306	10.8%
0.93	0.1691	0.0161	9.5%
0.97	0.0478	0.0051	10.6%

For $T_r < 0.95$, there is a relevant discrepancy between theoretical and numerical values. Note that the lower the reduced temperature, the greater the difference between the interfacial tensions for the same temperature. A possible cause for this effect would be numerical errors in the calculation of gradients, which are accentuated the lower the temperature and the higher the value of κ.

It was not possible to perform the test on model 1B satisfactorily, as the pressure is constant in the whole domain. Therefore, results for model 1B will not be presented in this section.

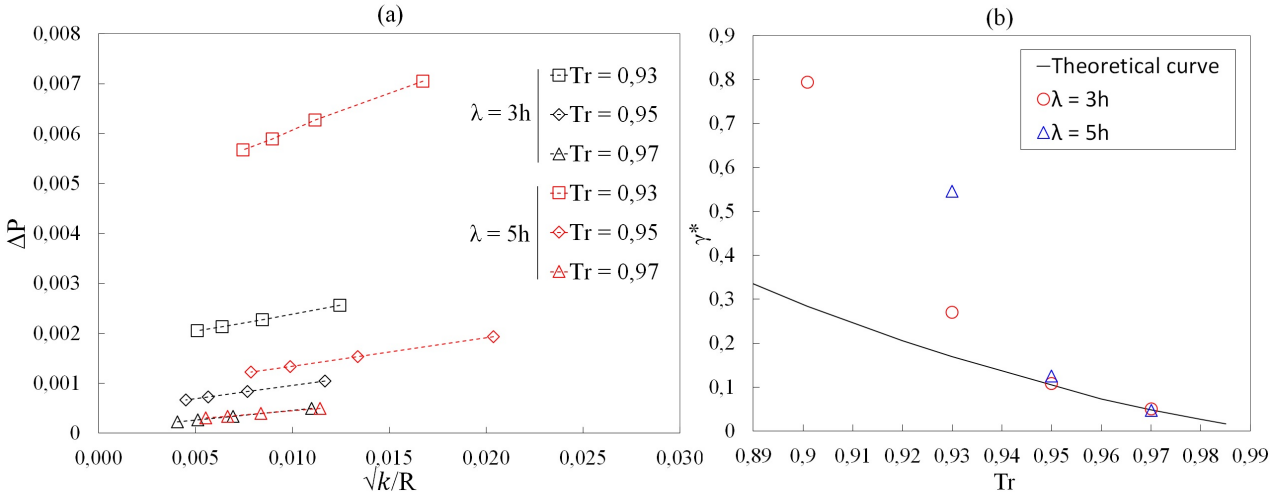

Figure 8. (a) Young-Laplace test for model 1A; (b) Comparison between the numerical surface tension and the theoretical values, for Model 1A.

Figure 9(a) shows the Young-Laplace test for the model 2. The interface tension obtained is similar to the theoretical curve, with a small deviation from the expected values, as seen in Fig. 9(b). The results presented by Siebert *et al.* (2014) suggest that the difference between numerical and theoretical values is due to the discretization order of the advective term.

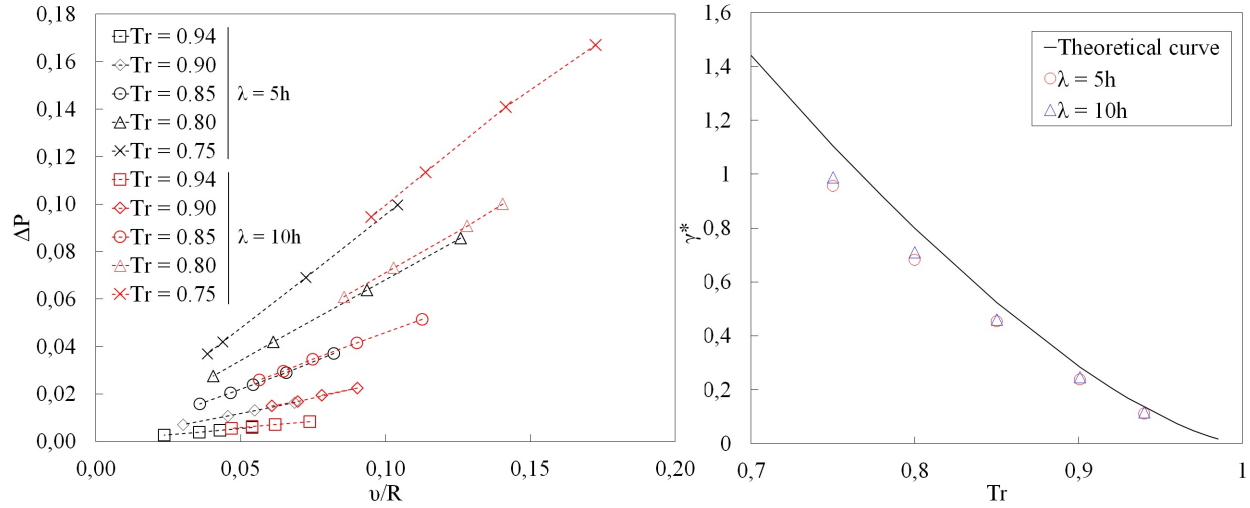

Figure 9. (a) Young-Laplace test for model 2; (b) Comparison between the numerical surface tension and the theoretical values, for Model 2.

3.5 Phase transition

One of the desirable features for liquid-vapor models is the ability to describe the phase transition in a fluid. To evaluate the models regarding this feature, it was performed an isothermal phase change simulation. The situation is similar to the vaporization of a liquid inside a cylinder with a piston. However, the simulation domain is truncated, so that the piston is outside the domain, and the vapor exits at a constant rate across an open boundary.

The boundary conditions used were periodic on the right and left, and bounce-back non-slip on the lower limit. At the upper limit, an open boundary with a fixed prescribed velocity was established. As an initial condition, the lower half of the domain was filled with liquid and the upper half with vapor.

The simulation was performed for a reduced temperature $T_r = 0.97$, and the domain height was 256h. The steam exit velocity is constant, $u_{LS} = 0.002$, so the interface displacement velocity u_{int} reads as $u_{int} = \frac{\rho_h^* u_h^* - \rho_l^* u_l^*}{\rho_h^* - \rho_l^*}$, where u_h^* is the velocity of the liquid phase and u_l^* is the velocity of the vapor phase (Lee and Lin, 2003).

Figure 10 shows the behavior of model 1A and model 2. For model 1A, it is possible to observe that there was a phase change, maintaining a sharp interface, which followed the predicted displacement. Nonetheless, it is noticeable a small

difference between the initial and final densities. Model 2 performed the phase transition with a sharp interface and kept the initial densities. On the other hand, model 1B could not perform phase change satisfactorily.

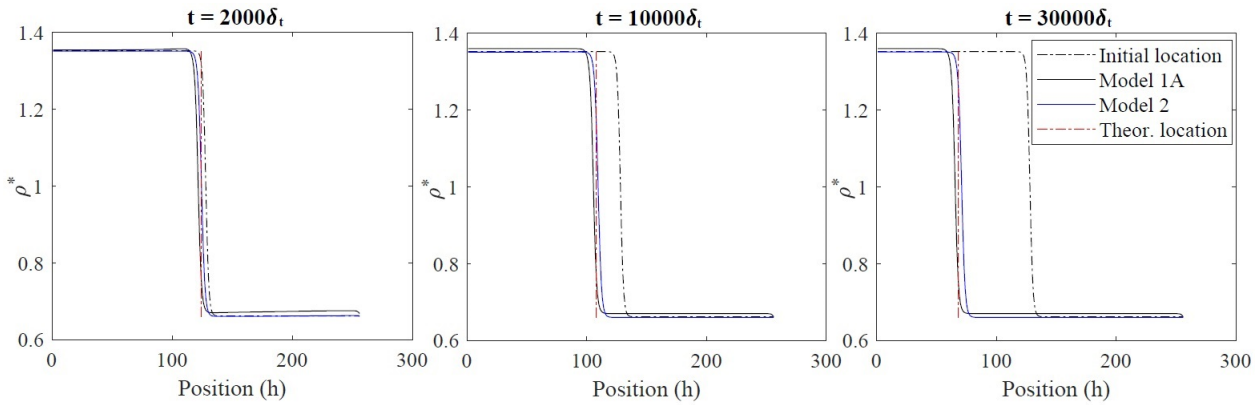

Figure 10. Density profile for models 1A and 2 during phase transition, in comparison with the predicted location of the interface.

3.6 Rayleigh-Taylor Instability

For this simulation, the boundary conditions were non-slip bounce-back at the upper and lower limits and periodic conditions at the left and right limits.The domain begins with the upper half filled with dense fluid, with a perturbation A, described by $A = A_o \cos(2\pi x/W)$, where the initial perturbation $A_o = 0.1W$, and wavelength equals to domain width W.

Until this moment, it was not reached a typical mushroom-shaped IRT with model 1A and model 2. However, model 1B obtained results consistent with those of He *et al.* (1999), as shown in Fig. 11.

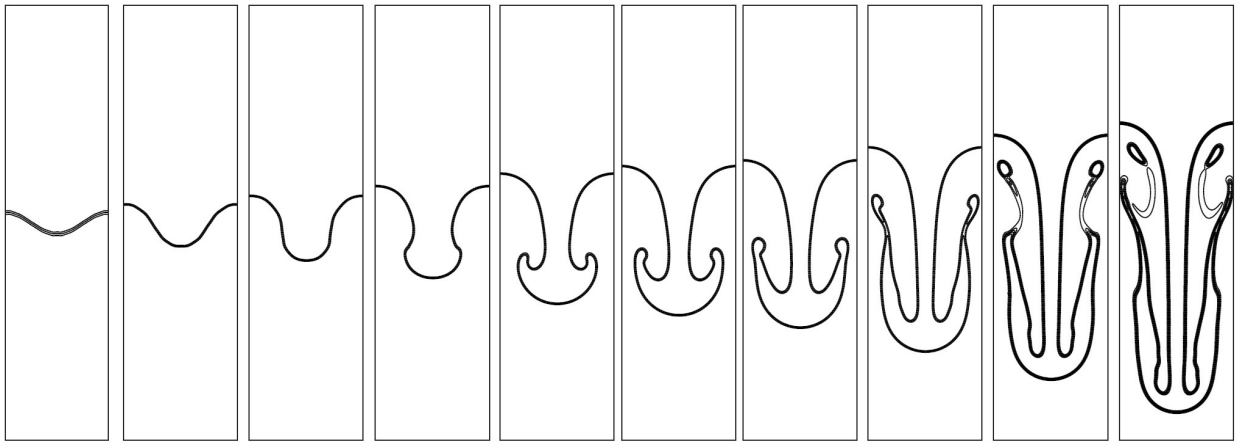

Figure 11. Rayleigh Taylor instability, for a 128x512 domain, with $T_r = 0.93$, gravity set to 1.25×10^{-5} and $\nu = 0.015$.

As pointed by Zhang *et al.* (2000), Chao *et al.* (2011), Huang *et al.* (2015) and other authors, model 1's pressure P^* is not well defined. Although the definition $P^* = \psi^* + \rho^* c_s^2$ implies that Eq. 18 and Eq. 19 are equivalent, the simulation results demonstrate two distinct models. In this sense, the pressure P^* obtained by Eq. 14 does not correspond to the thermodynamic pressure, but the hydrostatic pressure.

In a flow where the Stokes hypothesis is valid, that is, when the volume viscosity of a fluid is zero, the viscous stress tensor trace is also zero.This means that hydrostatic pressure is equal to thermodynamic pressure. However, from a discrete point of view, the thermodynamic pressure will only be equal to the hydrostatic pressure when the kinetic energy is an equilibrium moment.

Considering that model 1 is a second-order model, employing the D2Q9 velocity set, the viscous tension tensor trace will not necessarily be zero. Therefore, thermodynamic pressure and hydrostatic pressure are different. That may be one of the possible sources of divergence between models 1A and 1B.

4. CONCLUSIONS

In model 1, due to He *et al.* (1999), two calculation alternatives were identified. For the alternative A, the simulations showed instabilities at the interface and presence of artificial interface tension. With this calculation method it was not possible to simulate Rayleigh-Taylor instability, but it performed phase transition well. On the other hand, the simulations obtained by alternative B was able to simulate a Rayleigh-Taylor instability, but it showed appreciable anisotropy at the interface and the model does not follow the Laplace Law.

It was possible to observe similarities between model 1A and model 2, proposed by Siebert *et al.* (2014). The models employ similar strategies to introduce intermolecular interactions and they recover equivalent macroscopic equations. On the other hand, model 2 employs a higher-order velocity set. This implies different improvements in the model, including the proper calculation of gradients, contributing to the isotropy and stability of the interface (Siebert *et al.*, 2014).

The theoretical difference between model 1A and 1B is still unclear. Third-order errors that differentiate thermodynamic pressure from hydrostatic pressure may be a possible source of divergence between models.To better investigate this, it can be used a correction term for the pressure as a function of the viscous tensor.

5. ACKNOWLEDGEMENTS

The first author would like to acknowledge and thank CNPq (Conselho Nacional de Desenvolvimento Científico e Tecnológico) for the financial support.

6. REFERENCES

Chao, J., Mei, R., Singh, R. and Shyy, W., 2011. "A filtered-based, mass-conserving lattice bltzmann method for immiscible multiphase flows". *International Journal for Numerical Methods in Fluids*, pp. 622–647.

He, X., Chen, S. and Zhang, R., 1999. "A lattice boltzmann scheme for incompressible multiphase flow and its applications in resolution of reyleigh-taylor instability". *Journal of Computational Physics*, pp. 642–663.

He, X., Shan, X. and Doolen, G.D., 1998. "Discrete boltzmann equation for nonideal gases". *Physical Review E*.

Huang, H., Sukop, M. and Lu, X., 2015. *Multiphase Lattice Boltzmann Methods: Theory and Application*. John Wiley & Sons, New Jersey.

Inamuro, T., Ogata, R., Tajima, S. and Konishi, N., 2004. "A lattice boltzmann method for incompressible two-phase flows with large density differences". *Journal of Computational Physics*, pp. 628–644.

Kikkinides, E.S., Yotis, A.G., Kainourgiakis, M.E. and Stubos, A.K., 2008. "Thermodynamic consistency of liquid-gas lattice boltzmann methods: Interfacial property issues". *Physical Review E*.

Kruger, T., Kusumaatmaja, H., Kuzmin, A., Shardt, O., Silva, G. and Viggen, E.M., 2017. *The Lattice Boltzmann Method: Principles and Practice*. Springer International Publishing Switzerland.

Lee, T. and Lin, C.L., 2003. "Pressure evolution lattice-boltzmann-equation method for two-phase flow with phase change". *Physical Review E*, Vol. 67.

Lee, T. and Lin, C.L., 2005. "A stable discretization of the lattice boltzmann equation for simulation of incompressible two-phase flows at high density ratio". *Journal of Computational Physics*, pp. 16–47.

Philippi, P.C., 2022. *Lectures on Thermodynamics*. To be published.

Philippi, P.C., Mattila, K.K., Siebert, D.N., Santos, L.O.E., Junior, L.A.H. and Surmas, R., 2012. "Lattice-boltzmann equations for describing segregation in non-ideal mixtures". *Journal of Fluid Mechanics*, pp. 564–587.

Shan, X. and Chen, H., 1994. "Simulation of nonideal gases and liquid-gas phase transitions by the lattice boltzmann equation". *Physical Review A*, Vol. 49.

Siebert, D.N., Philippi, P.C. and Mattila, K.K., 2014. "Consistent lattice boltzmann equations for phase transitions". *Physical Review E*, Vol. 90.

Swift, M.R., Orlandini, E., Osborn, W.R. and Yeomans, J.M., 1996. "Lattice boltzmann simulations of liquid-gas and binary fluid systems". *Physical Review E*.

Tryggvason, G., 1988. "Numerical simulations of the rayleigh-taylor instability". *Journal of Computational Physics*, Vol. 75, pp. 253–282.

Zhang, R., He, X. and Chen, S., 2000. "Interface and surface tension in incompressible lattice boltzmann multiphase model". *Computer Physics Communications*, pp. 121–130.

7. RESPONSIBILITY NOTICE

The authors are solely responsible for the printed material included in this paper.